

ARTICLES

Proton-proton analyzing power and spin correlation measurements between 250 and 450 MeV at $7^\circ \leq \theta_{c.m.} \leq 90^\circ$ with an internal target in a storage ring

B. v. Przewoski,^{1,2} F. Rathmann,^{2,*} W. A. Dezarn,^{1,†} J. Doskow,¹ M. Dziedzic,¹ W. Haeberli,² J. G. Hardie,^{1,‡} B. Lorentz,² H. O. Meyer,¹ P. V. Pancella,³ R. E. Pollock,¹ T. Rinckel,¹ F. Sperisen,¹ and T. Wise²

¹Department of Physics, Indiana University, Bloomington, Indiana 47405

and Indiana University Cyclotron Facility, Bloomington, Indiana 47405

²University of Wisconsin-Madison, Madison, Wisconsin 53706

³Western Michigan University, Kalamazoo, Michigan 49008

(Received 18 May 1998)

We have measured the pp spin correlation coefficients A_{xx} , A_{yy} , A_{xz} and the analyzing power A_y at 250.0, 280.0, 294.4, 310.0, 350.0, 399.1, and 448.9 MeV over the laboratory angular range 3.5° – 43.5° ($\theta_{c.m.} = 7^\circ$ – 90°). The statistical accuracy is approximately ± 0.006 for A_y and ± 0.02 for A_{mn} per 1° angle bin, while the corresponding scale factor uncertainties are 1.3 and 2.5 %, respectively. The experiment makes use of a polarized hydrogen gas target internal to a proton storage ring (IUCF Cooler) and a circulating beam of polarized protons. The method of calibration relative to pp spin correlation coefficients and analyzing power at 197.4 MeV, the injection energy, involves up and down ramping of the energy of the polarized beam. The data are compared to recent pp partial waves analyses and NN potential models, emphasizing in particular the energy dependence in the region of the pion production threshold. [S0556-2813(98)01510-6]

PACS number(s): 13.88.+e, 24.70.+s, 13.75.Cs, 25.40.Cm

I. INTRODUCTION

We reported the first use of an internal polarized hydrogen gas target in a proton storage ring to measure A_{xx} , A_{yy} , A_{xz} , and A_y at 197.8 MeV between $4.5^\circ \leq \theta_{lab} \leq 17.5^\circ$ in Ref. [1]. Subsequently, we upgraded the detector system to allow measurements over the full angular range $3.5^\circ \leq \theta_{lab} \leq 43.5^\circ$ [2]. The present paper describes the measurement of complete angular distributions of the spin correlation coefficients A_{xx} , A_{yy} , A_{xz} and the analyzing power A_y at 250.0, 280.0, 294.4, 310.0, 350.0, 399.1, and 448.9 MeV. In these measurements, beam was stored at 197.4 MeV, then accelerated to the energy of interest. Data were accumulated at *both* energies, in order to be able to relate the polarization calibration at the higher energy to the known calibration at 197.4 MeV. The analysis of the data at the injection energy together with a detailed description of the experimental apparatus as well as the method of data acquisition and analysis are presented in Ref. [2]. The emphasis of the present paper is on the energy dependence of pp scattering in the vicinity of the pion production threshold. It also deals with those aspects of experimental technique and data analysis which

explicitly depend on energy. The present experiment provides data with high statistical accuracy and small systematic errors as a test of potential models and as input to phase shift analyses. The data were accumulated during two weeks separated into two running periods. This measurement also provides a polarization standard for protons from 200 to 450 MeV. This standard is presently used in a series of experiments in pion production with polarized beam and polarized hydrogen target [3].

An overview of the experimental apparatus and data acquisition and processing will be given in Secs. II–VI. Systematic uncertainties are discussed in Sec. V. The calibration export to the higher energies is described in Sec. VI. The resulting calibration standard is discussed in Sec. VII. In Sec. VIII the spin correlation parameters are compared to theory, followed by summary and outlook in Sec. IX.

II. EXPERIMENTAL ARRANGEMENT

A. Overview over the polarized internal target experiment (PINTEX) apparatus

The experiment is mounted in the A region of the Indiana Cooler. In this location the dispersion almost vanishes and the horizontal and vertical betatron functions are small [4], allowing the use of a narrow target cell. The target setup consists of an atomic beam source [1,5] which injects polarized hydrogen atoms into a storage cell with thin teflon walls [1,2]. Elastically scattered protons are detected in coincidence by a detector system consisting of scintillators, wire chambers, and silicon recoil detectors.

*Present address: Physikalisches Institut der Universität Erlangen-Nürnberg, D-91058 Erlangen, Germany; working at Forschungszentrum Jülich GmbH, D-52425 Jülich, Germany.

†Present address: Wake Forest University School of Medicine, Winston-Salem, NC 27157.

‡Present address: Christopher Newport University, Newport News, VA 23601.

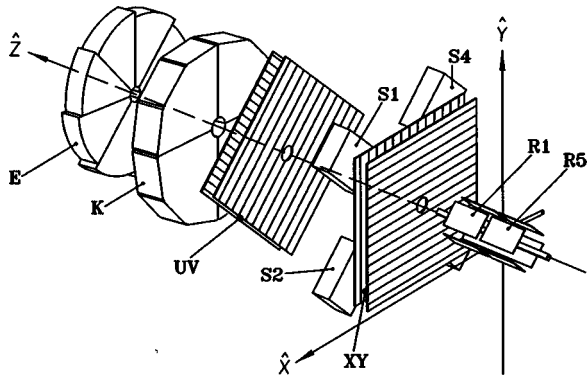


FIG. 1. Perspective view of the experimental setup. The components are described in the text.

B. Detector system

The detector setup is shown in Fig. 1. Only the general features are described here, for a more detailed description see Ref. [2].

Scattered protons in the angular range $3^\circ \leq \theta_{\text{lab}} \leq 35^\circ$ were detected as coincidences between the forward, segmented *E* detector (*E*) or the segmented *K* detector (*K*) and one of the eight position sensitive, 1 mm thick silicon strip detectors R1-8 mounted alongside the target cell. The silicon detectors stop recoil protons up to ~ 12 MeV. At 450 MeV incident energy the recoil energy is as high as ~ 50 MeV. Use of the thickest commercially available, fully depleted silicon detectors made it possible to still separate the recoil proton signals from detector noise.

C. Event type definition

Different combinations of the elements of the detector setup were used to define *pp* scattering events. We distinguish the following event types.

Type I a: Coincidences between the forward *E* or *K* detector and one of the eight position-sensitive silicon detectors R1-8. Forward scattered protons in the angular range $5^\circ \leq \theta_{\text{lab}} \leq 35^\circ$ passed through at least one of the two wire chambers (*XY* or *UV*). Between angles $5^\circ \leq \theta_{\text{lab}} \leq 8^\circ$ forward scattered protons passed only through the *UV* chamber.

Type I b: Events, for which the forward going proton is scattered at angles $\theta_{\text{lab}} \leq 5^\circ$, have no wire chamber information. These events are coincidences between the forward *E* detector and one of the eight position-sensitive silicon detectors R1-8. The forward going proton passes through the central hole of *both* wire chambers *and* the *K* scintillator before it is detected by the *E* scintillator further downstream. The scattering angle for these events is calculated from the calibrated energy of the recoiling proton which is stopped in one of the silicon detectors. The forward scattering angle up to which the recoil is stopped in the silicon detector is energy dependent. At 200 MeV it is 13° and at 450 MeV it is 8° in the laboratory.

Type II: Scattered protons in the angular range $30^\circ \leq \theta_{\text{lab}} \leq 60^\circ$ were detected as coincidences between two opposite elements of the S1-S4 scintillators. The hit position on the face of the detectors is determined from a position measurement by the *XY* wire chamber.

Note, that for a limited angular range both event types I a and II are possible. Similarly, there exists an angular range where the events can be analyzed either as type I a or type I b. These so-called ‘‘overlap regions’’ provide internal consistency checks for the data analysis.

D. Target

The target cell has a $10 \text{ mm} \times 10 \text{ mm}$ square cross section and a length of 25.4 cm. Polarized atoms are injected into the center of the teflon-walled cell. The target thickness is $2 \times 10^{13} \text{ H/cm}^2$.

The target cell is centered within an array of Helmholtz coils which provide horizontal, vertical, and longitudinal holding fields of about 0.3 mT for alignment of the target polarization [1,2]. The guide fields were kept at the same values for all energies. A more detailed account of the target characteristics and performance can be found in [1,2].

III. DATA ACQUISITION AND PROCESSING

A. Cooler cycle and spin handling

The beam from the cyclotron was injected into the Cooler at 197.4 MeV. The fill time was typically three minutes. The injection energy was chosen to be above the intrinsic depolarizing resonance near 180 MeV. Injection rates were on the order of $50 \mu\text{A}/\text{min}$. After injection, data were taken at 197.4 MeV for 48 s. This data taking period will be referred to as PRE. Then the beam was accelerated to an energy between 250 and 450 MeV where data were taken for 240 s. This period will be referred to as HE. At the end of the HE period, the beam was decelerated to 197.4 MeV where data were taken once more for 72 s. This period will be referred to as POST. At the end of this data acquisition cycle the polarization of the stored beam was reversed using a so-called spin flipper [6,7]. Next, the beam polarization at the polarized ion source was reversed and additional beam was injected to add to the beam remaining in the ring. In this manner, the sign of the beam polarization was alternating from cycle to cycle *and* we were able to keep the remaining beam at the end of the cycle. Thus, beam was accumulated over subsequent cycles and reached currents as high as 0.5 mA.

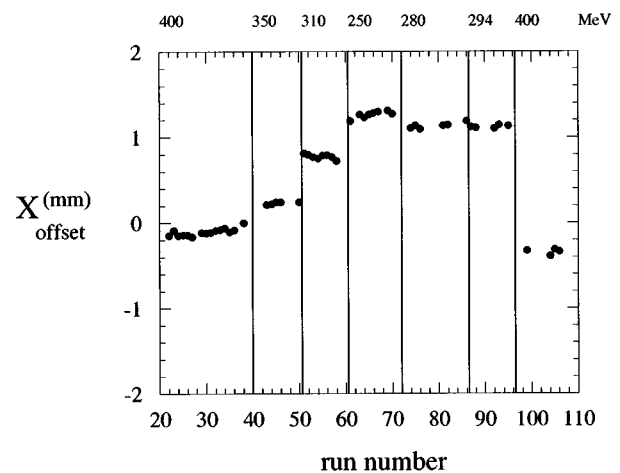


FIG. 2. Horizontal misalignment of the beam relative to the wire chambers as a function of beam energy.

The target spin was changed every 2 s, cycling through the sequence left, right, down, up, along, and opposite to the beam axis. This 12 s subcycle was repeated throughout the data taking phases.

B. Detector geometry with respect to the beam

The approximate wire chamber positions were surveyed optically prior to the experiment. Because the directions of the two coincident protons are constrained by kinematics, the exact detector positions, relative to the beam, could be extracted from the data, to correct the surveyed positions.

Retuning the ring after an energy change can result in a slightly altered beam position at the target. Thus, some of the corrections to the geometry are energy dependent. As an example, the software offset necessary to correct for the alignment of the X wire chamber with respect to the beam is shown in Fig. 2. Changes in beam energy are indicated. Similar software offsets were determined for the three other wire chamber planes and the radial distances of the silicon detectors. A detailed description of the determination of these software offsets can be found in [2].

C. Identification of pp events (kinematic fitting)

Events with the forward proton at angles larger than 5° in the laboratory were evaluated by performing, for every event, a minimum χ^2 fit constrained by elastic scattering kinematics. Input to the fitting routine were wire chamber and silicon position information. This fitting procedure made no use of the pulse height information of the silicon or scintillator detectors (see [2]).

For event type I b the scattering angle had to be determined from the calibrated pulse height [2] of the stopped recoil protons. In the angular range where the scattering angle could be determined from either the silicon pulse height or the wire chamber information, agreement within 0.06° was found at all energies. For event type II the kinematic fitting procedure tested events against the energy-dependent opening angle *and* coplanarity, since wire chamber information was available for both prongs.

D. Software cuts

1. Energy-independent cuts

For a given event the quality of agreement with *pp* elastic scattering kinematics is reflected in the χ^2 value of the fit. To compare events with different degrees of freedom, a fixed value of the integral over the tail of the probability density function $P(\chi^2, \nu)$ (i.e., a fixed ‘‘confidence level’’) was used. Events of type I a and type II were accepted if the calculated statistical probability $P(\chi^2, \nu) \leq 0.8$. See also Sec. V B 3 for details on this particular choice of cutoff.

The azimuthal detector acceptance was limited in software to four intervals, centered at $\phi_i = (\pm 45^\circ, \pm 135^\circ)$ including a ϕ range of $\pm 18.5^\circ$. This limit is within the physical acceptance of the silicon detectors.

2. Energy-dependent cuts

For type I a events the correlation between energy loss in the recoil detector and the forward scattering angle was used to place an additional constraint on the data. Two-

dimensional, energy-dependent software gates were used to identify the locus [2]. The cut on the probability that an event obeyed elastic scattering kinematics was chosen to be the most restrictive. Consequently, a relatively wide software gate was chosen to identify the locus in the θ_{forward} vs T_{recoil} spectrum [2].

IV. PROCESSING OF YIELDS

A. Diagonal scaling

The method of diagonal scaling [8] has been applied to analyze the data. The steps of this analysis are as follows.

We measure yields in four ϕ intervals centered at ϕ_i where ($i = 1 \dots 4$). The orientation of the target polarization Q is either horizontal, vertical, or longitudinal. The beam polarization P is always vertical. For each orientation (x, y, z) of the target polarization, data in four polarization states of beam and target were taken ($++, +-, -+, --$) where the two signs correspond to the sign of the beam and the target polarization, respectively. Let ($k = 1 \dots 4$) be the index of the four polarization states.

With A_y and A_{mn} being functions of the scattering angle θ , a set of 16 yields is obtained for each interval of the scattering angle $\Delta\theta$ and for each of the three possible target orientations. For each $\Delta\theta$ the measured yields can be written as

$$Y_{ik} = \epsilon_i \cdot (\sigma_{ik}) \cdot \lambda_k, \quad (4.1)$$

where ϵ_i is the detector efficiency for each quadrant, λ_k is the accumulated luminosity in each polarization state, and σ_{ik} is the spin-dependent cross section.

Since the sums of rows and columns of the matrix of interest σ_{ik} are constrained, ‘‘diagonal scaling’’ can be employed to find diagonal matrices $(\epsilon_i)^{-1}$ and $(\lambda_k)^{-1}$ such that $\sigma_{ik} = (\epsilon_i)^{-1} Y_{ik} (\lambda_k)^{-1}$ is a matrix with the known constraints. After ‘‘scaling,’’ the matrix σ_{ik} can be used to determine the experimental quantities $P_y \cdot A_y$, $Q_x \cdot A_y$, $Q_y \cdot A_y$, $P_y \cdot (Q_x + Q_y) \cdot A_{xx}$, $P_y \cdot (Q_x + Q_y) \cdot A_{yy}$, and $P_y \cdot (Q_x + Q_y) \cdot A_{xz}$. In the following, we will refer to these products of polarization \times observable as PQR numbers.

B. Determination of A_y , A_{xx} , A_{yy} and A_{xz}

The analyzing power and spin correlation coefficients as well as beam and target polarizations can be determined from the PQR numbers. The yields in the overlap region of event types I a and II ($30^\circ - 35^\circ$ in the laboratory) were added prior to diagonal scaling. Between 5° and 7° in the laboratory, where the scattering angle could be determined independently from either the wire chambers or the recoil energy, we chose to calculate the arithmetic mean of the analyzing power and spin correlation coefficients obtained from analyzing the events either as type I a or type I b. We retained the larger of the two errors after averaging. The procedure to normalize to both analyzing power and spin correlation coefficients of our earlier experiment [1] is described in Sec. VI.

Aside from the observables of interest and the ‘‘wanted’’ polarization components, the procedure of diagonal scaling also determines the so-called ‘‘unwanted’’ polarization com-

TABLE I. Upper limits of corrections and systematic uncertainties for all energies and angles.

Corrections and systematic uncertainties	magnitude	
corrections:		
θ -bin centroid	≤ 0.005	
ϕ -centroid shift	≤ 0.01	
systematic uncertainties:		
background	$\leq 1/3$	of the statistical error
θ vs energy correlation	$\leq 1/3$	of the statistical error
cut on $P(\chi^2, \nu)$	$\leq 1/4$	of the statistical error, type I a
	$\leq 1/2$	of the statistical error, type II
deadtime	$\leq 1/5$	of the statistical error
software offsets	$\leq 1/20$	of the statistical error
θ calibration	$\pm 0.06^\circ$	

ponents. Unwanted components are the small components of the beam polarization other than vertical, and of the target polarization other than along the direction of the active holding field. Some of the unwanted polarization components are nonflipping, which means that their sign is not reversed upon reversal of either beam or target polarization. These nonflipping components allow for a change in magnitude of the polarization after reversal, and are taken into account to first order in the analysis. Information about the relative size of the unwanted components can be found in [2].

C. Corrections

The final data are evaluated in 1° wide angular bins $\Delta\theta$. A correction of at most 0.005 was applied to obtain the value of the observables at the bin center.

Deviations from the ideal azimuthal acceptance were determined from the measured spin-averaged ϕ distribution of the processed events. Shifts of the ϕ centroids away from the ideal values of $\pm 45^\circ$ and $\pm 135^\circ$, assumed in diagonal scaling, resulted in a correction of the A_{mn} by at most 0.01. A detailed account of the procedure to center the θ angle bin as well as the correction for nonuniform ϕ acceptance can be found in [2].

V. SYSTEMATIC UNCERTAINTIES

Here, we discuss various systematic uncertainties. A summary is given in Table I.

A. Background

Background from the walls of the storage cell is a concern, since the material of the cell walls is many orders of magnitude thicker than the gas inside the cell. A detailed description of the procedure to determine the background contribution can be found in [2].

The admixture of background, which passed the kinematic constraints imposed to filter out the events of interest, was inferred from measurements made with a N_2 target. In that case, the kinematic correlations which are characteristic for pp elastic scattering, disappear. The assumption is that

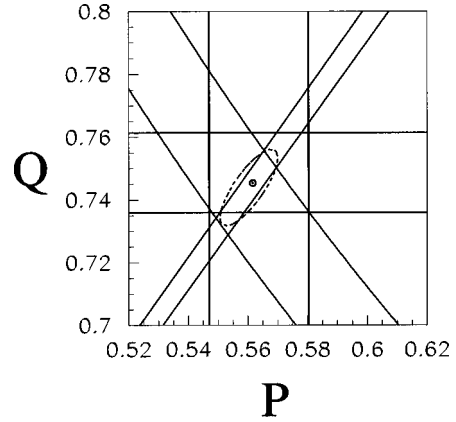


FIG. 3. Most probable choice of beam and target polarization P^* and Q^* at 350 MeV (dot). The lines indicate bands corresponding to one standard deviation of P , Q , (PQ) , and (P/Q) . The dashed line indicates the error of P^* and Q^* (70% confidence level contour).

for the purpose of a background measurement details of the nuclear structure become unimportant and N_2 behaves similar to C and F (the components of teflon).

The background is “energy dependent” because it depends on the machine tune, which determines the overlap of the beam halo with the cell walls. For this reason it is not surprising that the background reflects changes in transverse beam position as they are shown in Fig. 2. As mentioned earlier, the data were taken during two running periods, the first of which was entirely devoted to 450 MeV. Data at the other energies were taken during the second running period. The machine setup during the first running period was noticeably different from the one during the second running period.

With the cuts used for the final replay the background at 200 MeV was always $\sim 0.5\%$ for event type I a and $\sim 0.2\%$ for event type II. The background at 280 MeV was $\sim 1.1\%$ for event type I a and $\sim 0.6\%$ for event type II. At the other energies of this particular running period the background contribution was less. The smallest background was found at 350 MeV with $\sim 0.8\%$ for event type I a and $\sim 0.3\%$ for event type II.

At 450 MeV the background for event type I a was $\sim 3.2\%$ and $\sim 0.7\%$ for event type II. For event type I b, a background fraction of $\sim 3.5\%$ for the two smallest angle bins was found at 450 MeV. Note that this number is similar to the number obtained for the events with wire chamber information at the same energy. In addition, no systematic differences were found between the analyses using either the

TABLE II. Statistical relative uncertainty of the overall normalization of the analyzing power A_y at the different bombarding energies. At 197 MeV the uncertainty arises from the comparison to the reference data [1]. At the higher energies it also includes the uncertainty incurred in the calibration export. The normalization uncertainty of the spin correlation coefficients A_{mn} is twice the values listed.

T' (MeV)	197	250	280	294	310	350	400	450
$\delta k/k$ (%)	0.31	1.08	0.89	1.17	1.01	1.03	0.86	1.00

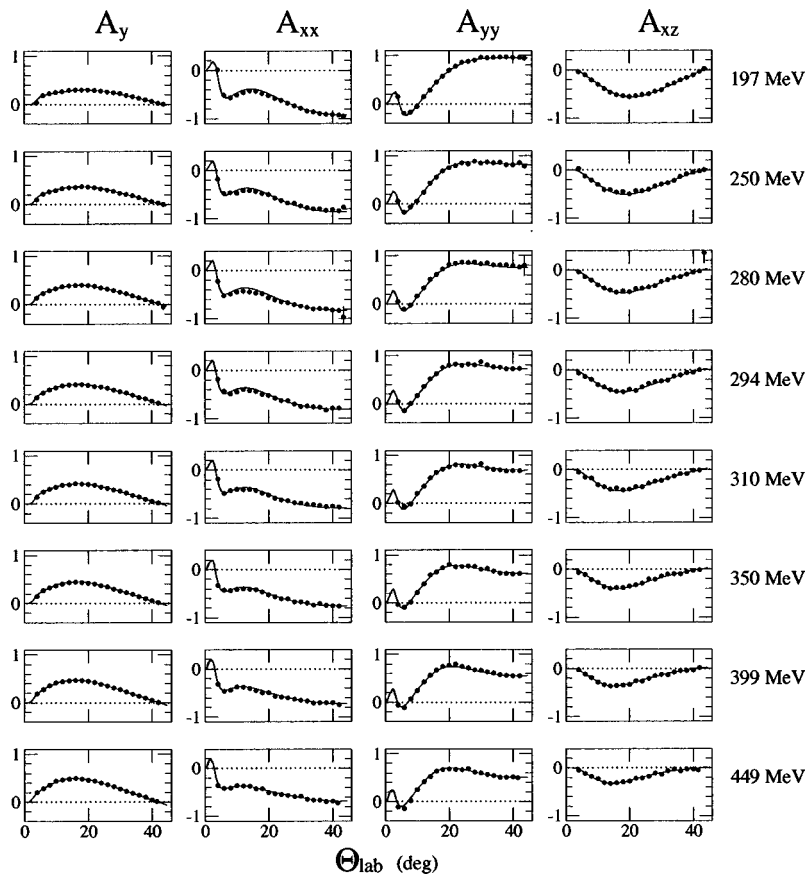


FIG. 4. Analyzing power and spin correlation coefficients as function of energy and angle. The curves are the SM97 phase shift analysis.

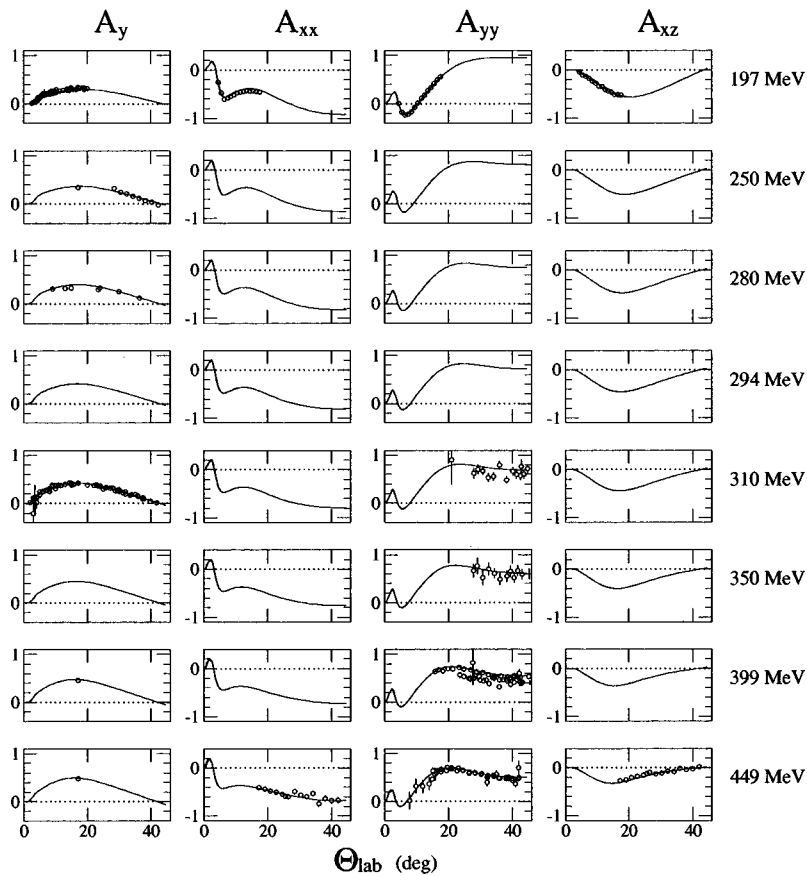


FIG. 5. All previously existing data between 175 MeV and 475 MeV from the SAID data base. The axes are the same as in Fig. 4. The references from the SAID data base are listed in Ref. [25] The curves are the SM97 phase shift analysis.

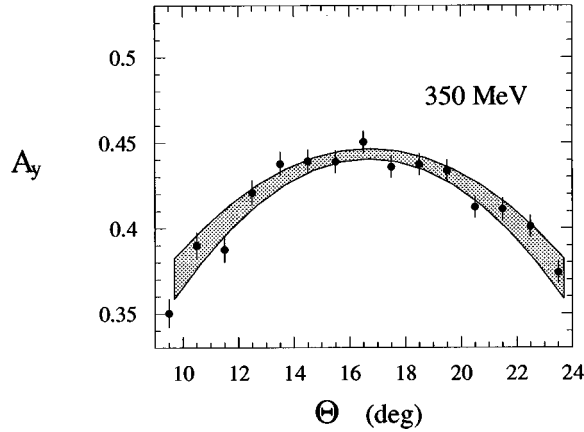


FIG. 6. Analyzing power maximum at 350 MeV. The shaded area is the error corridor (one standard deviation) of a parabolic fit to the data.

recoil energy or the wire chamber information for angles where the recoiling proton was stopped in the silicon detector.

The uncertainty of the background contribution is $\pm 0.05\%$ for event types I a,b and $\pm 0.02\%$ for event type II. The upper limit of the effect of the background admixture on A_y and A_{mn} was less than 1/3 of an error bar at all energies.

B. Sensitivity to software cuts

In order to quantify the effect of software cuts on A_y and A_{mn} we varied the cuts individually and calculated the associated change in A_y and A_{mn} . The sensitivity to the cuts was investigated as a function of angle.

1. Wire chamber multiplicities

The final data sample consists of events with a range of allowed wire chamber multiplicities. Ideally, a track has exactly one hit per wire chamber plane. The data sample was subdivided into two sets, one consisting only of events with ideal wire chamber multiplicities and the other consisting of events with all other allowed wire chamber multiplicities. For the latter, all possible wire combinations were tried and

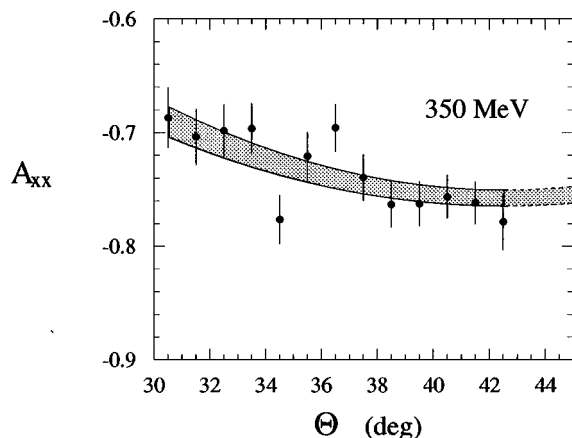


FIG. 7. Spin correlation coefficient A_{xx} at 350 MeV. The shaded area is the error corridor (one standard deviation) of a parabolic fit to the data.

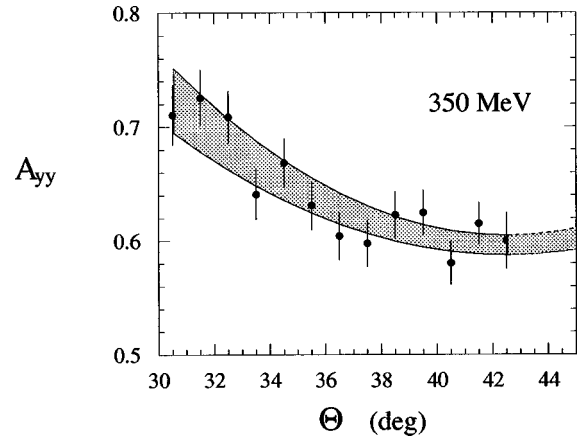


FIG. 8. Spin correlation coefficient A_{yy} at 350 MeV. The shaded area is the error corridor (one standard deviation) of a parabolic fit to the data.

the one with the smallest χ^2 from the kinematic fit was selected. The two sets gave statistically consistent results for both A_y and A_{mn} .

2. Angle vs energy correlation for event type I a

The relatively wide gate (Fig. 4 of Ref. [2]) on the kinematic locus of the angle of the forward proton as a function of the recoil energy was studied by replacing it by a gate about a factor of 2.5 smaller in area. The corresponding change in A_y and A_{mn} was less than 1/3 of their respective statistical uncertainties.

3. Quality criterion for the kinematic fit

The cut on $P(\chi^2, \nu)$ (see Sec. III D) was varied between 0.1 and 0.98. For event type I a the results are stable within ± 0.25 of the statistical error for probability cuts between 0.5 and 0.8. Above the limit of 0.8, background appears to affect the result. For example, the fraction of background increases from 3.2% (450 MeV, see Sec. V A) to 5.7% (type I a) and from 1.1 to 3.8% (type II), if the probability cut is relaxed to 0.98. For probability cuts below 0.5 either instrumental asymmetries affect the fitting procedure or statistical fluctuations for the very restricted data sample become important. For event type II the results were only stable within ± 0.5 of the statistical error for probability cuts 0.5–0.8. This is believed to be the case because no other restriction, such as the angle vs energy correlation for event type I a, is imposed on type II events. The probability cut of 0.8 was finally chosen for the analysis, because it significantly reduced the background. Placing the probability cut at 0.8 allowed us to retain the largest sample of elastic scattering events within the range where the data were insensitive to variations of the probability cut. Tightening the probability cut any further changed the result by less than 0.25 (0.5) of the statistical error for event type I a (II). These numbers are upper limits, since data at the energy with the least favorable background conditions and the best statistics was used.

C. Absolute calibration of the angle scale

The determination of the scattering angle from the kinematic fitting has an uncertainty of $\leq 0.08^\circ$. It was checked

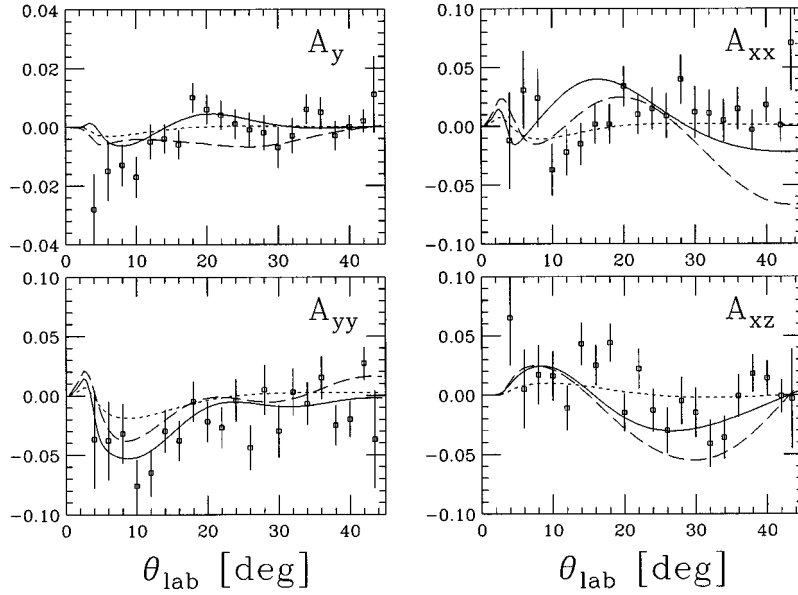


FIG. 9. Comparison of the present data at 250 MeV to partial-wave analyses. To make small effects more visible, we plot differences to a reference calculation. The reference is the Nijmegen partial-wave analysis (NI93). The curves shown correspond to the new Nijmegen analysis (dotted) and the old (dashed) and new (solid) VPI analysis (SM94, SM97).

against the zero crossing of the analyzing power at $\theta_{c.m.} = 90^\circ$. Linear fits to A_y near $\theta_{c.m.} = 90^\circ$ were performed at all energies. From these fits it was determined that the absolute scattering angle scale agrees with the expectation to $\pm 0.06^\circ$. This supports the correction of the distance of the wire chambers from the target which was discussed in Sec. III B.

D. Deadtime

A variation of the total rate in the detector for different combinations of beam and target polarization causes a spin dependence of the deadtime. The deadtime of the system was measured by scaling the number of triggers generated as well as the number of triggers actually processed by the com-

puter. In this manner a dead time correction was deduced for each polarization state separately. At all energies the effect of the deadtime correction would have been less than 20% of the statistical error and was therefore neglected.

E. Misalignment of the beam relative to the wire chambers

The systematic error arising from the uncertainty of the transverse wire chamber offsets, which reflect changes in beam position, was investigated. The A_y and A_{mn} were calculated twice for an energy where the offsets are large (on the order of 1 mm), once with the offsets applied and once with all offsets set to zero. The resulting effect on the observables was then scaled with the upper limit of the uncertainty of the wire chamber offsets, which is ± 0.05 mm. The

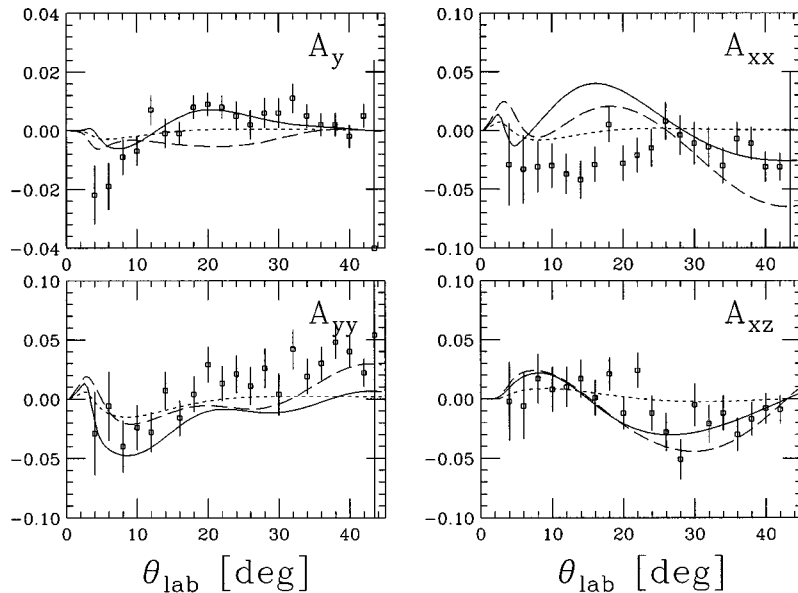


FIG. 10. Comparison of the present data at 280 MeV to partial-wave analyses. See caption of Fig. 9.

TABLE III. Maximum value of the analyzing power A_y^{\max} (results of a parabolic fit to the angular distribution). The first two columns give the bombarding energy in MeV, and the lab angle at which the maximum occurs. The uncertainties are from the following sources (1) statistical only, (2) error in the normalization to the reference data and due to the export the calibration from T_0 to T' , (3) normalization uncertainty of the reference data at 197.8 MeV (1.2% [1]). θ_{\max} results from the parabolic fit.

T' (MeV)	θ_{\max}	A_y^{\max}	$\delta A_y^{\max}(1)$	$\delta A_y^{\max}(2)$	$\delta A_y^{\max}(3)$
197.4	18.5	0.3044	± 0.0014	± 0.0009	± 0.0037
250.0	17.8	0.3687	± 0.0029	± 0.0040	± 0.0044
280.0	17.3	0.3986	± 0.0024	± 0.0035	± 0.0048
294.4	17.1	0.4068	± 0.0029	± 0.0048	± 0.0049
310.0	17.0	0.4182	± 0.0026	± 0.0042	± 0.0050
350.0	16.7	0.4435	± 0.0029	± 0.0046	± 0.0053
399.1	16.3	0.4660	± 0.0021	± 0.0028	± 0.0056
448.9	16.0	0.4893	± 0.0028	± 0.0049	± 0.0059

corresponding systematic errors are 3×10^{-4} for A_y and 1×10^{-3} for A_{mn} and thus negligible.

F. Absolute beam energy calibration

The beam energy is calculated from the ring frequency and the circumference of the ring (86.77 ± 0.01 m) [9]. The error in circumference translates into an absolute uncertainty of the beam energy of ± 200 keV.

G. Other effects

Here we briefly mention systematic effects that were already shown to be insignificant in [1]. Since the target cell was at the same position, centered within the same holding fields and only of slightly larger cross section, we assumed that there was no variation of the target polarization along the beam axis as during the previous measurement.

The effect of a beam motion which is correlated with the direction of the holding fields was shown to be negligible at 197.8 MeV [1]. Since the holding fields were kept at fixed values for all beam energies, the beam is bent less by the holding fields as the energy increases.

VI. CALIBRATION EXPORT

As explained earlier, each measurement cycle contains three data taking periods which we have labeled PRE, HE,

and POST. During the PRE period, data are acquired at the injection energy ($T_0 = 197.4$ MeV). The beam is then accelerated for data taking at the energy of interest T' (HE). Finally, the energy is lowered again for another measurement at T_0 (POST), all with the same stored beam. This sequence is repeated in every cycle.

In order to obtain the normalization of the polarization observables at T' , we compare the data at T_0 to the results of an earlier experiment [1] in which analyzing power and spin correlation coefficients were measured at 197.8 MeV. A small correction is applied to the data of Ref. [1] to account for the fact that the injection energy of the present experiment is 0.4 MeV lower. This results in a set of reference data $A_y^0(\theta_i)$, $A_{xx}^0(\theta_i)$, $A_{yy}^0(\theta_i)$, and $A_{xz}^0(\theta_i)$, where θ_i ranges from 8.5° to 17.5° in 1° wide bins.

The method of exporting a polarization calibration from one energy to another has been discussed in detail in a previous paper [10]. Here, we just summarize the main steps. As explained in Sec. IV A, diagonal scaling yields the products between polarizations and observables, at every angle, namely, $PA_y(\theta_i)$, $QA_y(\theta_i)$, and $PQA_{mn}(\theta_i)$. By scaling these angular distributions in the range from 8.5° to 17.5° to the reference data set, we obtain P^{PRE} , Q^{PRE} , P^{POST} , and Q^{POST} . Since the target polarization does not change during a cycle we can derive Q^{HE} immediately from the weighted average of Q^{PRE} and Q^{POST} . The next step involves the ratio

TABLE IV. Spin correlation coefficients A_{xx}^{90} and A_{yy}^{90} at $\theta_{cm} = 90^\circ$ (results of a parabolic fit to the angular distribution). The first two columns give the bombarding energy in MeV, and the lab angle θ_{\max} which corresponds to $\theta_{c.m.} = 90^\circ$ (calculated from kinematics). The three different uncertainties are described in the caption of Table III.

T'	θ_{\max}	A_{xx}^{90}	$\delta A_{xx}^{90}(1)$	$\delta A_{xx}^{90}(2)$	$\delta A_{xx}^{90}(3)$	A_{yy}^{90}	$\delta A_{yy}^{90}(1)$	$\delta A_{yy}^{90}(2)$	$\delta A_{yy}^{90}(3)$
197.4	43.57	-0.9326	0.0041	0.0057	0.0224	0.9613	0.0048	0.0059	0.0231
250.0	43.21	-0.8300	0.0077	0.0179	0.0199	0.8219	0.0092	0.0178	0.0197
280.0	43.01	-0.8259	0.0066	0.0147	0.0198	0.7799	0.0080	0.0139	0.0187
294.4	42.92	-0.8018	0.0075	0.0187	0.0192	0.7213	0.0090	0.0168	0.0173
310.0	42.81	-0.7633	0.0072	0.0154	0.0183	0.6692	0.0087	0.0135	0.0161
350.0	42.55	-0.7575	0.0070	0.0157	0.0182	0.5960	0.0085	0.0123	0.0143
399.1	42.24	-0.7179	0.0058	0.0124	0.0172	0.5470	0.0070	0.0095	0.0131
448.9	41.93	-0.6904	0.0073	0.0138	0.0166	0.4974	0.0088	0.0099	0.0119

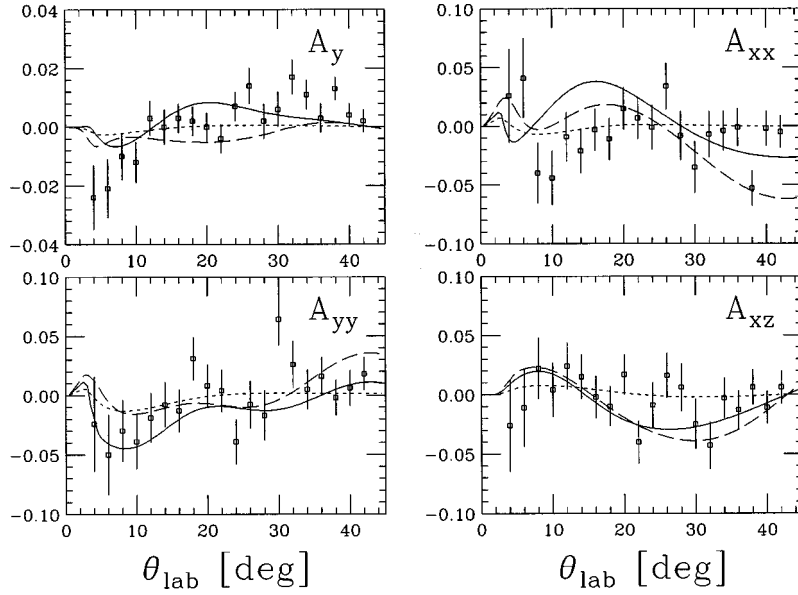


FIG. 11. Comparison of the present data at 294 MeV to partial-wave analyses. See caption of Fig. 9.

(P/Q) between the $PA_y(\theta_i)$ and $QA_y(\theta_i)$ distributions which, obviously, does not depend on A_y . For the PRE and POST periods, this ratio is derived from data in the angular range from 18.5° to 41.5° , i.e., a data sample that is not used for the comparison to the reference data set. For the HE period, the full angular range 8.5° to 41.5° is used to deduce $(P/Q)^{HE}$. From these ratios and the fact that the target polarization is constant over one cycle, we obtain information on the loss of beam polarization during the ramping of the beam energy. This loss is typically smaller than a few percent. A small correction is then applied to the known value of P and PQ during the PRE and POST periods, to arrive at the corresponding values P^{HE} and $(PQ)^{HE}$ during the HE period.

The above procedure thus results in four independent pieces of information about beam and target polarization during the measurement at T' , namely, P^{HE} , Q^{HE} , $(PQ)^{HE}$,

and $(P/Q)^{HE}$, and their statistical errors δP^{HE} , δQ^{HE} , $\delta(PQ)^{HE}$, and $\delta(P/Q)^{HE}$. For the analysis of the HE data, we are interested in the most probable choice of beam and target polarization P^* and Q^* which is obtained by minimizing the expression

$$\chi^2 = \frac{(P^{HE} - P^*)^2}{(\delta P^{HE})^2} + \frac{(Q^{HE} - Q^*)^2}{(\delta Q^{HE})^2} + \frac{[(PQ)^{HE} - P^*Q^*]^2}{[\delta(PQ)^{HE}]^2} + \frac{[(P/Q)^{HE} - P^*/Q^*]^2}{[\delta(P/Q)^{HE}]^2}. \quad (6.1)$$

This procedure is illustrated in Fig. 3, which shows, for the $T' = 350$ MeV case, the four conditions P^{HE} , Q^{HE} , $(PQ)^{HE}$, and $(P/Q)^{HE}$ as bands corresponding to \pm one standard deviation. As one can see, the four constraints are

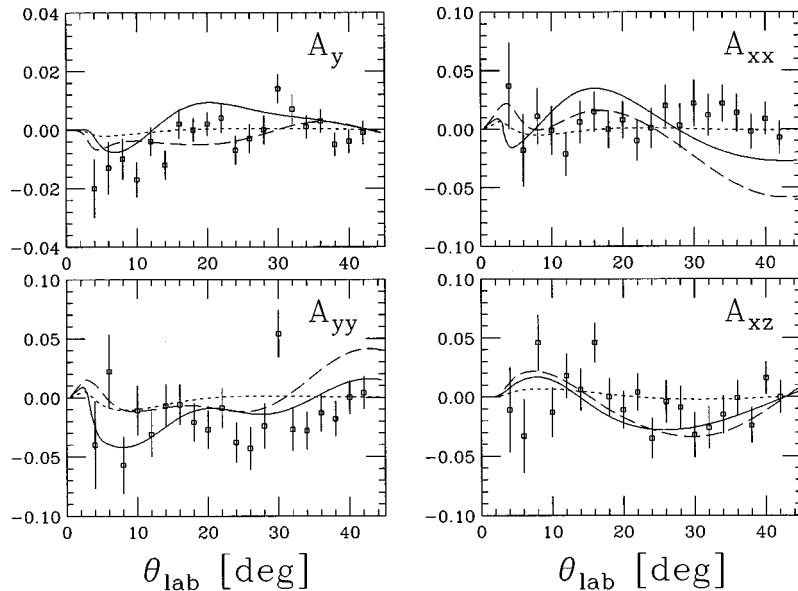


FIG. 12. Comparison of the present data at 310 MeV to partial-wave analyses. See caption of Fig. 9.

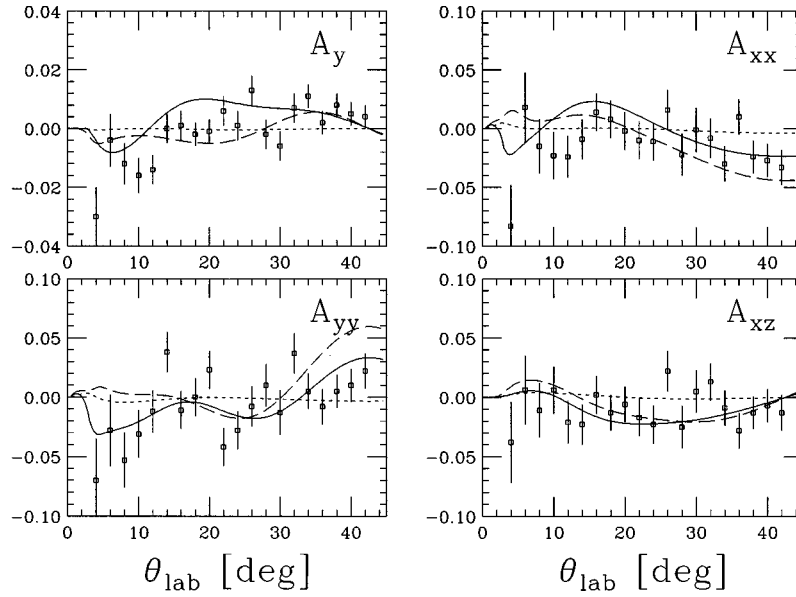


FIG. 13. Comparison of the present data at 350 MeV to partial-wave analyses. See caption of Fig. 9.

consistent among themselves. This means that the two independent ways to transport the calibration to the higher energy (either using the beam or the target polarization) are mutually consistent. The displayed point shows P^* , Q^* , as deduced by minimizing Eq. (6.1). The uncertainty of P^* and Q^* is shown by the dashed line (70% confidence level contour).

This procedure results in the most probable normalization of the A_y and A_{mn} angular distributions at a given energy, given the above constraints. It is important to realize that if one wanted to change the normalization of a set of A_y and A_{mn} data only a single number would be involved. If one, for example, renormalizes the analyzing power data by multiplying by a factor k , this necessarily means that the spin correlation coefficients have to be multiplied by k^2 (see Ref. [1]). We use this insight to arrive at the uncertainty δk of the

normalization, as follows. Clearly, k^2 is associated with the product P^*Q^* . The error, $\delta(P^*Q^*)$, is known from the minimization procedure. Thus, the normalization uncertainty is given by $\delta k = 0.5\delta(P^*Q^*)$. The values for δk are listed in Table II. They do not contain the normalization uncertainty δk° of the reference data set ($\delta k^\circ/k^\circ = 1.2\%$ [1]). A change of k° would simultaneously affect all results of this work.

VII. FINAL DATA

A. Angular distributions

The analyzing power and spin correlation coefficients from this experiment are shown in Fig. 4. The data, in 1° bins, can be found in tabular form on the PINTEX Web page

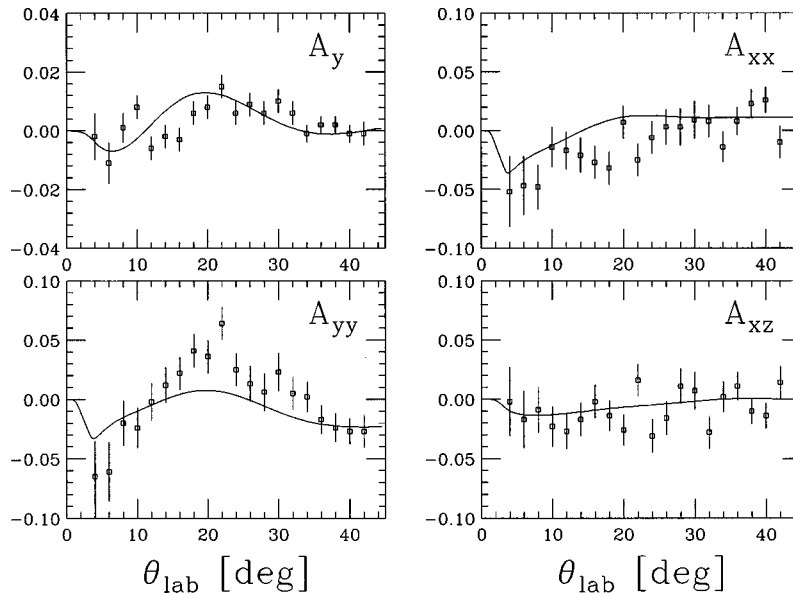


FIG. 14. Comparison of the present data at 399 MeV to partial-wave analyses. The reference (zero line) is the old (SM94) and the solid line the new (SM97) VPI analysis.

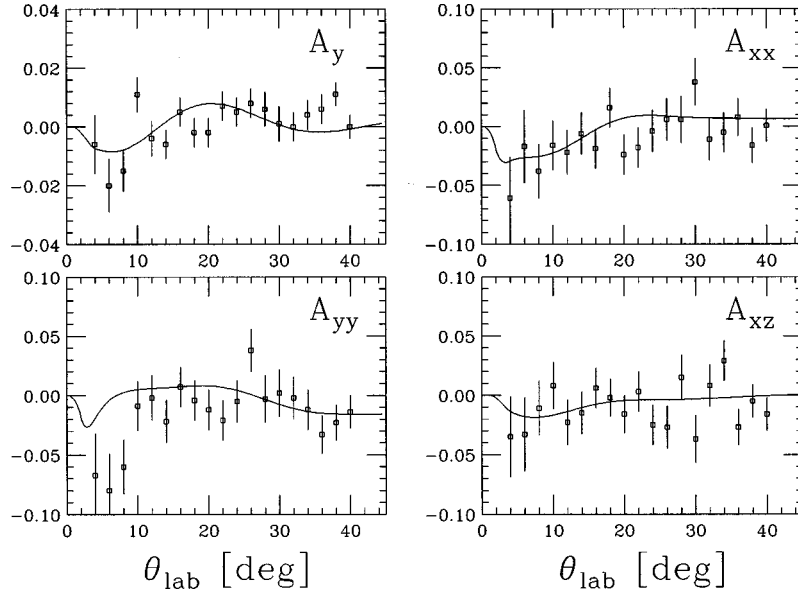


FIG. 15. Comparison of the present data at 450 MeV to partial-wave analyses. See caption of Fig. 14.

[11]. All previously existing analyzing power and spin correlation data between 175 and 475 MeV are shown in the same format in Fig. 5. The data are grouped in energy intervals centered at our energies, e.g., in the 250 MeV frames data at energies between 175 and 265 MeV are shown. As can be seen from Fig. 5, spin correlation data existed, with one exception, only for A_{yy} whereas analyzing power measurements were concentrated around 310 MeV, i.e., near the pion production threshold.

B. Extreme values as calibration standard

This measurement represents spin observables in pp elastic scattering with a known *absolute* normalization. It thus establishes a *polarization standard* between 200 and 450 MeV.

To facilitate the use of this standard by future experiments, we deduce in the following the value of observables at angles where the derivative vanishes. At these angles, the value of the observable is insensitive to the scattering angle, and the angular distribution near the extremum can be represented by a parabola which makes it possible to combine data over a certain angular range, thus lowering the statistical uncertainty. To this aim, we represent the observable $A(\theta)$ by the expression

$$A(\theta) = A^{\max} + a(\theta - \theta_{\max})^2, \tag{7.1}$$

where θ_{\max} and A^{\max} are the location and value of the maximum and a is the curvature of the parabola. The parameters of Eq. (7.1) are varied to minimize the usual χ^2 between Eq. (7.1) and the data. The number of data bins (1° wide) included in the fit is increased until the minimum χ^2 per point starts to increase indicating that the assumed parabolic shape is no longer valid. The stability of the fitted parameters is tested against a change in the number of data points included.

In the determination of the maximum of the analyzing power A_y^{\max} , all three parameters of Eq. (7.1) were varied. This was compared to a fit where the location θ_{\max} of the

maximum was fixed to the value given by a partial-wave analysis. The two results differed by much less than a statistical error bar. The curvatures, a , were found to vary smoothly with energy between 200 and 450 MeV. The total number of 1° data bins included ranged from 16 at 200 MeV to 14 at 350 MeV. In Fig. 6 the data near the maximum analyzing power and the error corridor of the associated fit are shown for 350 MeV.

The spin correlation coefficients A_{xx} and A_{yy} are symmetric around the center-of-mass angle of 90° . When deducing the extreme values A_{xx}^{90} and A_{yy}^{90} , only two parameters were varied (θ_{\max} was fixed to the lab angle which corresponds to $\theta_{c.m.} = 90^\circ$). The curvature in both cases was also found to be smooth with energy. The number of 1° data bins included was 20 for A_{xx} and 13 for A_{yy} at all energies. The spin correlation coefficients near $\theta_{c.m.} = 90^\circ$ and the error corridor of the fit at 350 MeV are shown in Figs. 7 and 8. As an additional check on the fitting procedure, the sum ($A_{xx}^{90} + A_{yy}^{90}$) and the difference ($A_{xx}^{90} - A_{yy}^{90}$) were compared with a parabolic fit to the angular distributions of the sum and difference of these observables, bin by bin, with consistent results.

The results are given in Tables III and IV. Three errors are listed: (1) the error of the fitted maximum value, reflecting the statistical uncertainty of the data, (2) the error from

TABLE V. χ^2 per datum for all observables ($A_y, A_{xx}, A_{yy}, A_{xz}$).

T (MeV)	197	250	280	294	310	350	399	449
SM94	5.3	2.0	1.9	1.7	1.9	1.5	1.6	1.2
SM97	2.5	1.3	2.0	1.4	1.5	1.3	1.3	1.2
NI93	1.8	1.3	1.6	1.3	1.3	1.3		
NI97	1.7	1.1	1.5	1.2	1.2	1.3		
CDBONN	1.9	1.1	1.7	1.3	1.3	1.8		
REID93	1.6	1.2	1.5	1.2	1.3	1.4		
AV18	2.7	1.2	1.6	1.3	1.5	2.3		
PARIS80	5.2	2.6	4.4	3.9	5.5	11.3		

TABLE VI. χ^2 per datum for all observables ($A_y, A_{xx}, A_{yy}, A_{xz}$) after adjusting the overall normalization k by the values shown in Table VII.

T (MeV)	197	250	280	294	310	350	399	449
SM94	5.2	1.9	1.8	1.7	1.8	1.5	1.5	1.2
SM97	2.1	1.3	1.8	1.4	1.3	1.3	1.3	1.2
NI93	1.5	1.3	1.3	1.3	1.2	1.3		
NI97	1.3	1.1	1.2	1.2	1.2	1.3		
CDBONN	1.4	1.1	1.2	1.2	1.3	1.7		
REID93	1.4	1.1	1.2	1.2	1.2	1.4		
AV18	2.1	1.2	1.4	1.3	1.5	2.3		
PARIS80	4.5	2.6	3.8	3.6	5.5	10.5		

the export of the normalization, and from the comparison to the reference data (this error is common to all data *at a given energy*, see Sec. VI), and (3) the intrinsic normalization uncertainty of the reference data set [1] which is common to all data in this report. Depending on the intended use of the calibration information, two or three of these errors have to be combined (in quadrature, since all three errors are independent and random).

VIII. COMPARISON OF THE DATA TO THEORY

A. Partial-wave analyses and NN potentials

The elastic scattering of protons on protons below the pion threshold is certainly one of the best known processes in nuclear physics. The wealth of measured observables has been summarized by partial-wave analyses in which the phase shifts of low angular momentum are treated as parameters while the higher angular momenta are supplied by a model of the long-range nucleon-nucleon (NN) interaction. Our work has resulted in a body of precise pp data of observables for which previously only few measurements have been carried out (compare Figs. 4 and 5). While no one ex-

TABLE VII. Normalization factor k , determined by scaling the present data as $k A_y$ and $k^2 A_{mn}$, in such a way that the overall χ^2 is minimized (the resulting χ^2 values are shown in Table VI).

T (MeV)	197	250	280	294	310	350	399	449
SM94	0.998	1.012	0.994	1.001	1.013	1.003	0.992	0.997
SM97	0.992	1.005	0.988	0.996	1.010	1.003	0.994	0.998
NI93	0.993	1.006	0.987	0.994	1.006	0.995		
NI97	0.991	1.005	0.987	0.994	1.006	0.995		
CDBONN	0.991	1.003	0.985	0.992	1.005	0.995		
REID93	0.993	1.006	0.988	0.995	1.007	0.998		
AV18	0.990	1.005	0.988	0.996	1.009	0.999		
PARIS80	0.989	1.003	0.985	0.991	1.001	0.987		

pects big surprises at this stage, such a body of data constitutes a real test of our current knowledge of pp scattering.

In the following, we will compare our data to the partial-wave analyses of the VPI and Nijmegen groups. From each group we have selected two energy-dependent solutions that are separated by about 3 years and reflect the progress still made in the characterization of the pp interaction. These modern partial-wave descriptions have now reached the stage where the χ^2 per datum is about 1. The particular solutions, used here, are the following.

SM94: The published partial-wave analysis of the VPI group [12]; range of validity 0–1600 MeV. Numerical values have been obtained from the SAID interactive program [13].

SM97: The recently published partial-wave analysis of the VPI group; range of validity 0–2500 MeV [14]. The numerical values have been obtained from the SAID interactive program [13]. In contrast to SM94, the data basis for this analysis contains analyzing power and spin correlation at 197.8 MeV which have been measured previously by our group [1].

NI93: The published partial-wave analysis of the Nijmegen group [15]; range of validity 0–350 MeV. The χ^2

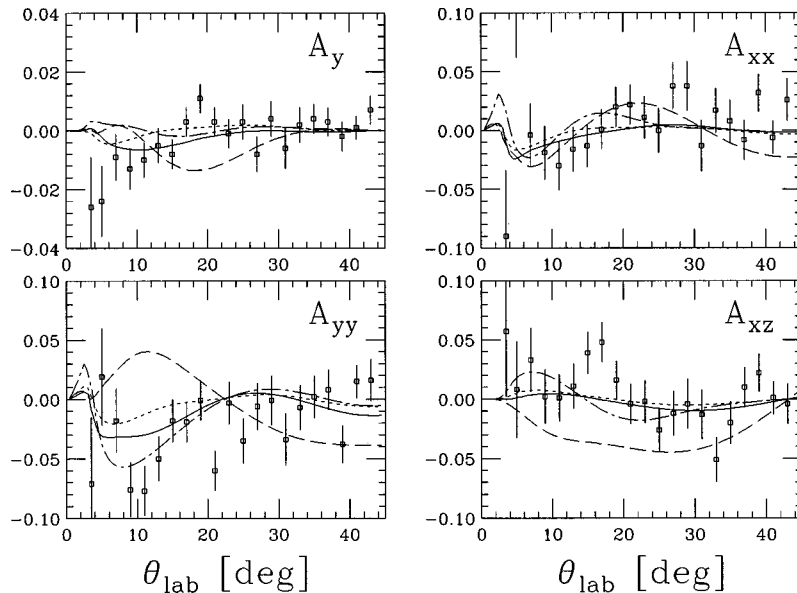


FIG. 16. Comparison of the present data at 250 MeV to NN potentials. The reference is the Nijmegen partial-wave analysis (NI93). The curves shown correspond to REID93 (dotted), AV18 (dot-dash), CDBONN (solid), and PARIS80 (dashed).

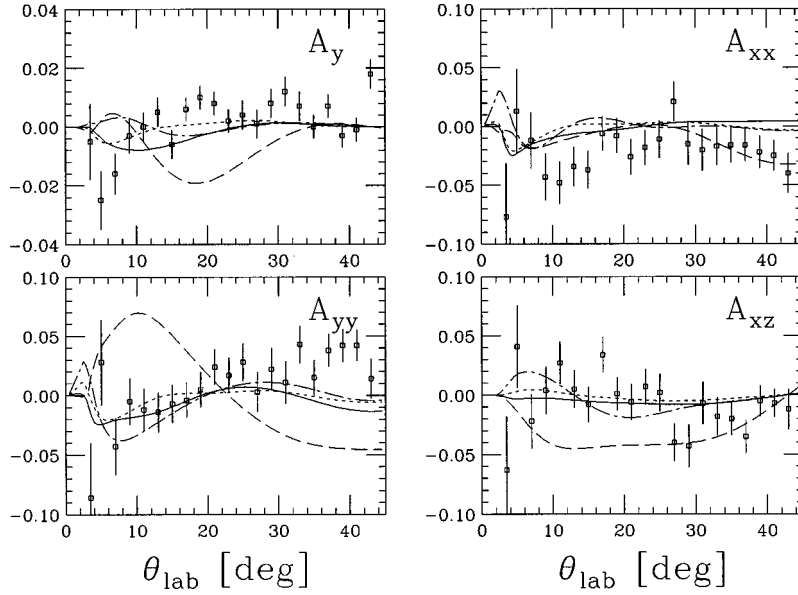


FIG. 17. Comparison of the present data at 280 MeV to NN potentials. See caption of Fig. 16.

per datum is 1.08. Numerical values have been obtained from Ref. [16].

NI97: The yet unpublished partial-wave analysis of the Nijmegen group. Numerical values have been obtained from Ref. [16]. In contrast to NI93, the data basis for this analysis contains analyzing power and spin correlation data at 197.8 MeV which have been measured previously by our group [1].

A comparison of the present data to the above partial-wave analyses is shown in Figs. 9–15. To make small effects more visible, we plot differences to a reference calculation. For Figs. 9–13, the chosen reference is NI93. Thus, the departure of the dotted line from zero illustrates four years of development of the Nijmegen partial-wave analysis. For the VPI analysis, time progresses from the dashed line (SM94) to the solid line (SM97). At the two highest energies (Figs. 14 and 15), only the VPI analysis is applicable. In this case,

the chosen reference is SM94. Thus, development is illustrated by the departure of the solid line (SM97) from zero.

We note, that in general, the difference between the VPI and the Nijmegen phase shift analysis has become smaller with time, at least for the observables discussed here. For a quantitative comparison, the overall χ^2 of all our data in relation to the four partial-wave analyses is listed in Table V. The improvement in χ^2 that would result from a free normalization of the present data at each energy are shown in Table VI. The corresponding normalization factors are listed in Table VII. These factors are all well within the experimental normalization error listed in Table II (except at 280 MeV where the normalization factor is about 0.988 and the error in Table II is 0.89%). We note that the new analyses of both groups have a smaller χ^2 than the corresponding earlier analyses. It is also interesting that for the Nijmegen analysis, the listed χ^2 per datum for the present data set is larger than

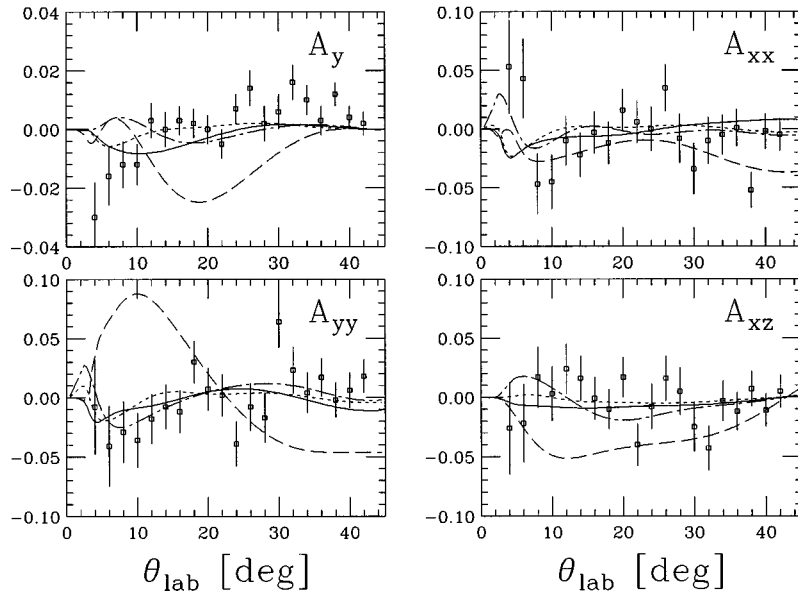


FIG. 18. Comparison of the present data at 294 MeV to NN potentials. See caption of Fig. 16.

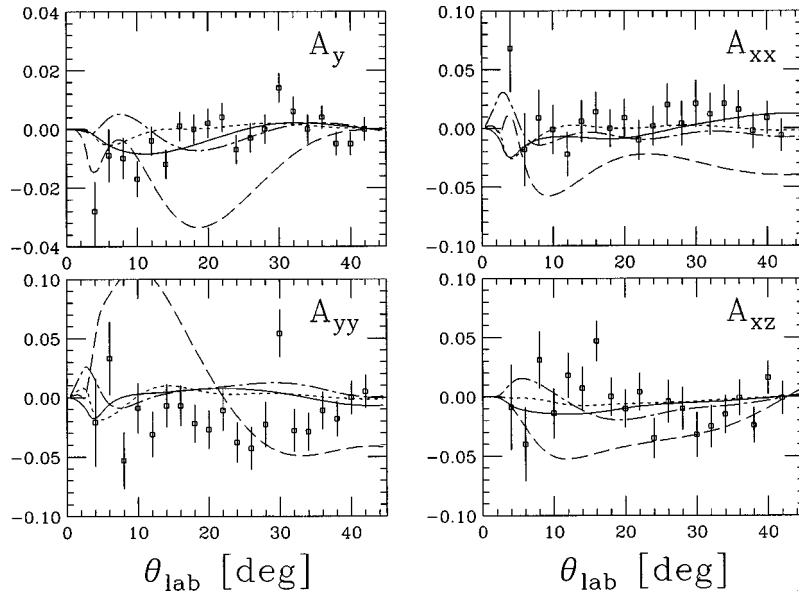


FIG. 19. Comparison of the present data at 310 MeV to NN potentials. See caption of Fig. 16.

the value for the whole data base (1.08).

For use in nuclear physics calculations it is necessary to provide a potential representation of the NN interaction. Over the years (since 1950) many NN potentials were constructed. A number of these potentials are compared with pp data below 350 MeV in Ref. [17]. Potentials are constructed to fit the data (pp and np), or directly the output of certain partial-wave analysis. It thus may seem superfluous to compare measurements also to potentials, but to a user of a potential it still might be interesting to know how well that potential reproduces double-spin data, in a sector where previously little data existed. It is also obvious that potentials which usually contain more physics constraints than partial-wave analyses give a less perfect fit of the data. It is thus of interest to test whether spin observables are particularly responsible for the deviation of the model from the data. From

the wealth of potential representations we have selected three modern NN potentials with varying constraints. For historic reasons and to document the progress made during the last 15 years, we also compare our data to the older, previously popular Paris potential. The particular potentials, used here, are the following.

REID93: One of the potentials of the Nijmegen group, discussed in Ref. [18]. The 1π -exchange potential is explicitly included, and the lower partial waves are individually adjusted, resulting in nonlocality (50 adjustable parameters). The χ^2 per datum for the whole data base is 1.03. The numerical values have been obtained from Ref. [16].

AV18: Updated Argonne potential [19]. It uses a free phenomenological form at short distance, but maintains a local operator structure (40 adjustable parameters). The χ^2 per datum for the whole data base is 1.09. The numerical values

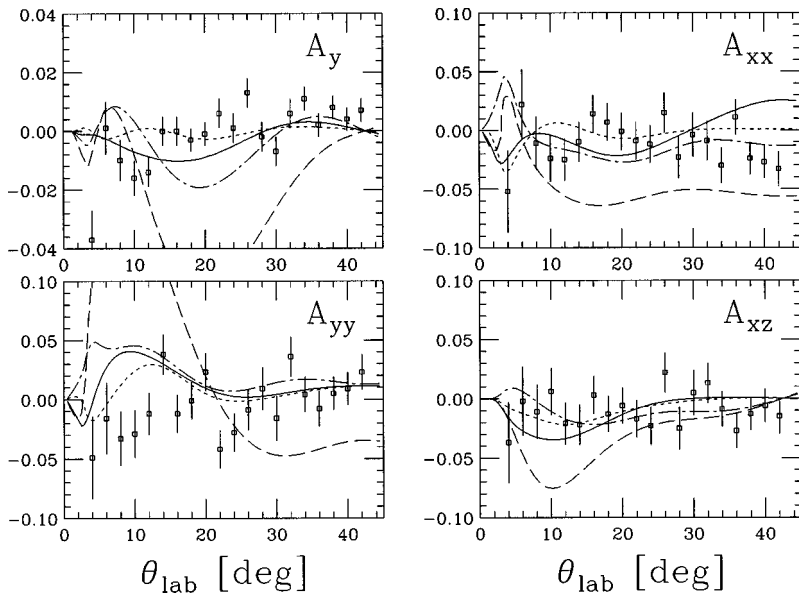


FIG. 20. Comparison of the present data at 350 MeV to NN potentials. See caption of Fig. 16.

have been obtained from Ref. [20].

CDBONN: The charge-dependent version of the Bonn potential [21]. Details of this potential have not yet been published, but numerical values are available through the SAID interactive program [13].

PARIS80: The Paris potential [22]. The numerical values have been obtained through the SAID interactive program [13].

The range of validity of all of the above potentials is from 0 to 350 MeV. A comparison of the present data to the above potential calculations is shown in Figs. 16–20. The overall χ^2 of all our data in relation to the above potentials is listed in Table V. Table VI shows the improvement in χ^2 that would result from a free normalization of the present data, and Table VII lists the corresponding normalization factors, which are all well within the experimental normalization error.

B. Energy dependence

In the middle of the energy range covered by this experiment, the production of pions becomes energetically possible. Of the four partial wave analyses mentioned above, two (SM94, SM97) are set up to deal with the onset of inelasticities, while the analysis of the Nijmegen group is not valid beyond 350 MeV, where the pion production cross section becomes sizeable. It is therefore interesting to compare the energy dependence of the present measurement with the predicted energy dependence of the partial-wave analyses.

The maximum value A_y^{\max} of the analyzing power as a function of energy is shown in Fig. 21. The data points are the same as listed in Table III, with uncertainties obtained by combining $\delta A_y^{\max}(1)$ and $\delta A_y^{\max}(2)$, but omitting the overall normalization uncertainty $\delta A_y^{\max}(3)$. The VPI and Nijmegen partial wave analyses, SM97 and NI93, are shown as solid and dashed lines, respectively. Similarly, Fig. 22 shows a particular combination of two of the spin correlation coefficients at $\theta_{c.m.} = 90^\circ$ from Table IV. For this comparison, we chose the ratio $(A_{xx}^{90}/A_{yy}^{90})$. Here, we use only the uncertainties $\delta A_{xx}^{90}(1)$ and $\delta A_{yy}^{90}(1)$, since in the ratio the normalization uncertainty at each energy cancels. Again, the VPI and

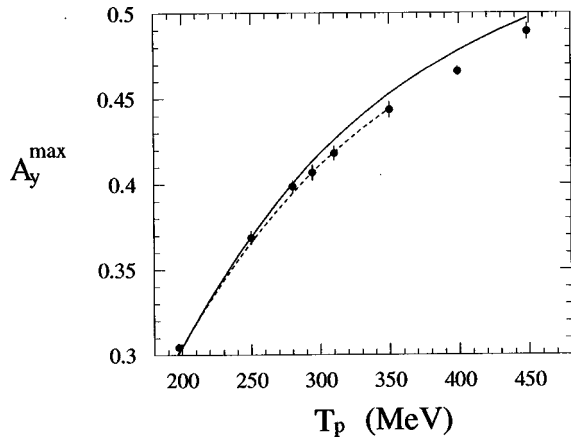


FIG. 21. Analyzing power maximum as obtained from the parabolic fits (see Fig. 6 for an example) as a function of energy. The dashed and the solid line are the NI93 partial-wave analysis and the SM97 partial-wave analysis, respectively.

Nijmegen partial wave analyses, SM97 and NI93, are shown as solid and dashed lines, respectively.

It is noteworthy that the agreement between the NI93 calculation and the data in both Figs. 21 and 22 is much better than is the case for the VPI analysis. This is likely to be attributed to the fact that the latter is constrained by the requirement of continuity towards energies beyond 350 MeV where the inelastic channels become significant, while the Nijmegen analysis does not deal with this energy range. It thus seems that in the pion threshold region a rapid energy variation is required which the global SM97 calculation is unable to reproduce. It is interesting that this discrepancy is more evident in the spin correlation data.

IX. SUMMARY AND OUTLOOK

We report measurements of analyzing power A_y and spin correlation coefficients A_{xx} , A_{yy} , and A_{xz} at 250.0, 280.0, 294.4, 310.0, 350.0, 399.1, and 448.9 MeV with an internal polarized gas target in the Indiana proton storage ring (Cooler). The present work extends the earlier measurements at 197.4 MeV to higher energies. Both protons were detected in coincidence over an angular range of $\theta_{c.m.} = 7^\circ - 90^\circ$. Kinematic fitting was employed to determine the scattering angle. The statistical accuracy is approximately ± 0.02 for A_{mn} and ± 0.006 for A_y per 1° angle bin. Systematic uncertainties are less than a third of the statistical error.

The most recent partial wave analyses are in good agreement with our data (overall $\chi^2/\text{point} = 1.2$) and modern potential models are approaching the same quality of fit. It should be noted, however, that the energy dependence of the Nijmegen potential does not join smoothly to higher energies (Figs. 21 and 22).

The data were taken in a new mode of operation where the beam was accelerated and decelerated in the same cycle. This mode, and the use of the polarized target, allowed us to export the known calibration at 197.4 MeV to the higher energies. The present data represent an independent, secondary calibration standard in the energy range 200–450 MeV. Their absolute normalization is based on a calibration point at 183 MeV [23] which, in turn, uses an $A_y = 1$ point in

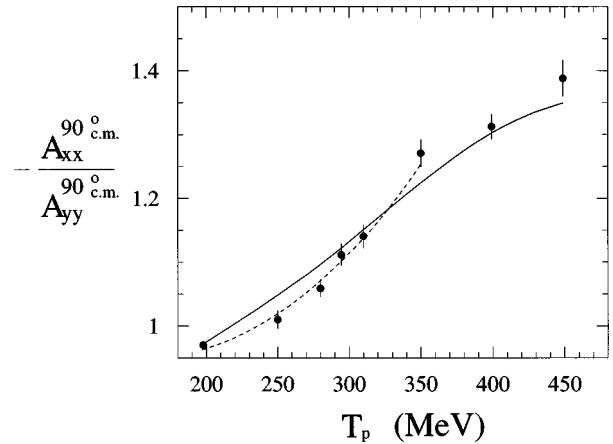


FIG. 22. Ratio of spin correlation coefficients at $\theta_{c.m.} = 90^\circ$ as a function of energy. The values come from a parabolic fit to the data, see Figs. 7, 8 for an example. The dashed and the solid line are the NI93 partial-wave analysis and the SM97 partial-wave analysis, respectively.

$^{12}\text{C}(p,p)^{12}\text{C}$ elastic scattering [24]. Future pion production experiments with the Indiana Cooler will utilize the present data as a calibration standard. The capability to ramp the beam energy up *and* down also resulted in an increase in luminosity by about a factor of 4, achieved by retaining the beam at the end of each cycle and adding more beam during the injection phase. The polarization of the stored beam was reversed once per cycle by adiabatic crossing of an induced depolarizing resonance.

The present measurement clearly demonstrates the advantage of the experimental technique with an internal polarized target in a storage ring with electron cooling. The highest bombarding energy of the present experiment is 450 MeV, because of the limited energy range of the Indiana Cooler. New spin correlation data between 450 and 2500 MeV are expected from COSY in the near future.

ACKNOWLEDGMENTS

We thank Dr. J. J. deSwart, Dr. M. C. M. Rentmeester, and Dr. V. G. J. Stoks for providing tables of numerical results for comparison to the present data, and for permission to include results from their as yet unpublished new phase shift analyses. We thank Dr. P. Thörnngren Engblom for maintaining the PINTEX web page [11]. We also thank Dr. J. Balewski for help with the statistical analysis. We are grateful for the untiring efforts of the accelerator operations group at IUCF, in particular G. East and T. Sloan. This work was supported in part by the National Science Foundation and the Department of Energy. One of us (F.R.) would also like to thank the Alexander von Humboldt Foundation for their generous support.

-
- [1] W. Haeblerli, B. Lorentz, F. Rathmann, M. A. Ross, T. Wise, W. A. Dezarn, J. Doskow, J. G. Hardie, H. O. Meyer, R. E. Pollock, B. v. Przewoski, T. Rinckel, F. Sperisen, and P. V. Pancella, *Phys. Rev. C* **55**, 597 (1997).
- [2] F. Rathmann, B. von Przewosi, W. A. Dezarn, J. Doskow, M. Dzemiđzic, W. Haeblerli, J. G. Hardie, B. Lorentz, H. O. Meyer, P. V. Pancella, R. E. Pollock, T. Rinckel, F. Sperisen, and T. Wise, *Phys. Rev. C* **58**, 658 (1998).
- [3] H. O. Meyer, *Annu. Rev. Nucl. Part. Sci.* **47**, 235 (1997).
- [4] M. A. Ross, W. K. Pitts, W. Haeblerli, H. O. Meyer, S. F. Pate, R. E. Pollock, B. von Przewoski, T. Rinckel, J. Sowinski, F. Sperisen, and P. V. Pancella, *Nucl. Instrum. Methods Phys. Res. A* **326**, 424 (1993).
- [5] T. Wise, A. D. Roberts, and W. Haeblerli, *Nucl. Instrum. Methods Phys. Res. A* **336**, 410 (1993).
- [6] D. D. Caussyn, Ya. S. Derbenev, T. J. P. Ellison, S. Y. Lee, T. Rinckel, P. Schwandt, F. Sperisen, E. J. Stephenson, B. von Przewoski, B. B. Blinov, C. M. Chu, E. D. Courant, D. A. Crandell, W. A. Kauffman, A. D. Krisch, T. S. Nurushev, R. A. Phelps, L. G. Ratner, V. K. Wong, and C. Ohmori, *Phys. Rev. Lett.* **73**, 2857 (1994).
- [7] B. von Przewoski, W. A. Dezarn, J. Doskow, J. G. Hardie, H. O. Meyer, R. E. Pollock, T. Rinckel, F. Sperisen, W. Haeblerli, B. Lorentz, F. Rathmann, T. Wise, and P. V. Pancella, *Rev. Sci. Instrum.* **67**, 165 (1996).
- [8] H. O. Meyer, *Phys. Rev. C* **56**, 2074 (1997).
- [9] H. O. Meyer, C. Horowitz, H. Nann, P. V. Pancella, S. F. Pate, R. E. Pollock, B. von Przewoski, T. Rinckel, M. A. Ross, and F. Sperisen, *Nucl. Phys.* **A539**, 633 (1992).
- [10] R. E. Pollock, W. A. Dezarn, M. Dzemiđzic, J. Doskow, J. G. Hardie, H. O. Meyer, B. v. Przewoski, T. Rinckel, F. Sperisen, W. Haeblerli, B. Lorentz, F. Rathmann, T. Wise, and P. V. Pancella, *Phys. Rev. E* **55**, 7606 (1997).
- [11] PINTEX homepage at URL <http://www.iucf.indiana.edu/Experiments/PINTEX/pintex.html>
- [12] R. A. Arndt, I. I. Strakovsky, and R. L. Workman, *Phys. Rev. C* **50**, 2731 (1994).
- [13] The SAID dial-in: available via TELNET to clsaid.phys.vt.edu, with userid:said (no password required).
- [14] SM97 R. A. Arndt, C. H. Oh, I. I. Strakovsky, R. L. Workman, and F. Dohrmann, *Phys. Rev. C* **56**, 3005 (1997).
- [15] V. G. J. Stoks, R. A. M. Klomp, M. C. M. Rentmeester, and J. J. de Swart, *Phys. Rev. C* **48**, 792 (1993).
- [16] J. J. de Swart (private communication).
- [17] V. G. J. Stoks and J. J. de Swart, *Phys. Rev. C* **47**, 761 (1993).
- [18] V. G. J. Stoks, R. A. M. Klomp, C. P. F. Terheggen, and J. J. de Swart, *Phys. Rev. C* **49**, 2950 (1994).
- [19] R. B. Wiringa, V. G. J. Stoks, and R. Schiavilla, *Phys. Rev. C* **51**, 38 (1995).
- [20] V. G. J. Stoks (private communication).
- [21] R. Machleidt, *Phys. Rev. C* **53**, 1483 (1996).
- [22] M. Lacombe, B. Loiseau, J. M. Richard, R. Vinh Mau, J. Ct, P. Pirs, and R. de Tournel, *Phys. Rev. C* **21**, 861 (1980).
- [23] B. von Przewoski, H. O. Meyer, P. V. Pancella, S. F. Pate, R. E. Pollock, T. Rinckel, F. Sperisen, J. Sowinski, W. Haeblerli, W. K. Pitts, and J. S. Price, *Phys. Rev. C* **44**, 44 (1991).
- [24] S. W. Wissink, S. P. Wells, E. J. Stephenson, J. Sowinski, A. D. Bacher, P. Li, J. Lisanti, C. Olmer, A. K. Opper, R. Sawafta, and P. Schwandt, *Phys. Rev. C* **45**, R504 (1992).
- [25] References from SAID data base. Chamberlain *et al.*, *Phys. Rev.* **95**, 1348 (1954); Baskir *et al.*, *ibid.* **106**, 564 (1957); Chamberlain *et al.*, *ibid.* **105**, 288 (1957); Abashian *et al.*, *Phys. Rev. Lett.* **1**, 255 (1958); Ashmore *et al.*, *Proc. Cambridge Philos. Soc.* **72**, 289 (1958); Allaby *et al.*, *ibid.* **77**, 234 (1961); Tinlot *et al.*, *Phys. Rev.* **124**, 890 (1961); Gotow *et al.*, *ibid.* **127**, 2206 (1962); Engels *et al.*, *ibid.* **129**, 1858 (1963); Vasilevskii *et al.*, *Sov. Phys. JETP* **18**, 3 (1964); Kazarinov *et al.*, *ibid.* **20**, 565 (1965); Etz *et al.*, *Phys. Rev.* **148**, 1289 (1966); Marshall *et al.*, *ibid.* **150**, 1119 (1966); Cheng *et al.*, *ibid.* **163**, 1470 (1967); Beretvas *et al.*, *ibid.* **171**, 1392 (1968); Axen *et al.*, *Lett. Nuovo Cimento* **20**, 151 (1977); Amsler *et al.*, *Nucl. Phys.* **4**, 1047 (1978); Bugg *et al.*, *J. Phys. G* **4**, 1025 (1978); Greeniaus *et al.*, *Nucl. Phys.* **A322**, 308 (1979); Besset *et al.*, *ibid.* **A345**, 435 (1980); Besset *et al.*, *Phys. Rev. D* **21**, 580 (1980); McNaughton *et al.*, *Phys. Rev. C* **24**, 1778 (1981); Aprile *et al.*, *Phys. Rev. D* **28**, 21 (1983); Onel *et al.*, *ibid.* **40**, 35 (1989); von Przewoski *et al.*, *Phys. Rev. C* **44**, 44 (1991); Pitts *et al.*, *ibid.* **45**, 455 (1992); von Przewoski *et al.*, IUCF, 9 (1995); Haeblerli *et al.*, *Phys. Rev. C* **55**, 597 (1997).